Aerospace Science and Technology 117 (2021) 106941

Contents lists available at ScienceDirect

Aerospace Science and Technology

www.elsevier.com/locate/aescte

Performance analysis of a strut-aided hypersonic scramjet by full-scale IDDES modeling

Wei Yao [a,b,*], Hang Liu [a,b], Lianjie Xue [a,b], Yabing Xiao [a,b]

[a] Key Laboratory of High-Temperature Gas Dynamics, Institute of Mechanics, CAS, Beijing 100190, China
[b] School of Engineering Science, University of Chinese Academy of Science, Beijing 100049, China

ARTICLE INFO

Article history:
Received 24 January 2021
Received in revised form 31 May 2021
Accepted 2 July 2021
Available online 12 July 2021
Communicated by Kai Liu

Keywords:
Hypersonic combustion
Hydrogen
Improved Delayed Detached Eddy Simulation (IDDES)
Dynamic zone flamelet model
Scramjet

ABSTRACT

The uninstalled performance of a full-scale scramjet operating over Mach 7 to 10 and altitudes of 28 to 40 km was numerically analyzed by using high-fidelity Improved Delayed Detached Eddy Simulation (IDDES) with 125.10 million cells and Dynamic Zone Flamelet model (DZFM) with 21,294 flamelet zones. The inviscid thrust can be well correlated with dynamic pressure in the form of a gaussian function, whereas the viscous drag increases almost linearly with dynamic pressure. For the examined scramjet, net thrust is achieved for the low dynamic pressure range below 37 kPa and the high range above 55 kPa. The rule of mixed is burnt is observed, and the final combustion efficiencies vary from 66% to 82%. The upstream propagation of combustion occurs for most of the cases in the current strut-based combustor, and unstart occurs for the case of Mach 7 at 30 km.

© 2021 Elsevier Masson SAS. All rights reserved.

1. Introduction

The pursing of a scramjet engine that can operate across the Mach region of 6 to 15+ has been devoted for more than 40 years and has never been given up even with extreme difficulty [1,2]. Almost permanent research efforts in developing an airbreathing vehicle flying at high Mach number have been pursued internationally, mainly by the USA, Japan, Europe, and China, since thirty years ago [3]. Scramjets that can work at extremely high flight Mach numbers are especially desirable for reusable space transportation systems and military systems [3]. Conceptual analysis indicates that hydrogen-fueled scramjet engines have the potential operational limit of Mach 15-16 [4]. Currently, the maximum speed of an airframe-integrated, scramjet-powered vehicle was achieved during the test of X-43A [5]. The third flight test of X-43A in 2004 successfully reached Mach 10 at an altitude of 33 km.

Hypersonic test facilities, e.g., NASA HYPULSE shock tunnel [4] and JAXA HIEST free-piston driven shock tunnel [6], capable of duplicating flight Mach from 7 to 15, were built to advance the high-Mach airbreathing propulsion techniques. The full-scale engine used to power the X-43A was developed and systematically evaluated in the NASA HyPulse Shock Tunnel at conditions duplicating Mach 10 flight. Currently, reflected-shock and shock-expansion tunnels are the two main approaches to generate the high-enthalpy test flows at Mach above 8.

The main challenge in designing a high-Mach scramjet is to reduce both the inviscid (pressure) and viscous (skin friction) drag while maintaining enhanced mixing and rapid combustion and minimizing total pressure losses. Due to the fact that the relative difference between engine inlet and nozzle exit velocity decreases at high Mach numbers [7], more drag is induced relative to the thrust, e.g., a net thrust of 1 is obtained at the thrust-drag-ratio of 7/6 at Mach 8. Therefore the optimization of combustion performance should be coupled with the drag evaluation. Due to the interactions between inlet, combustor, nozzle, and even part of the forebody, component-level studies can not predict the global performance of the overall scramjet engine. Also, because the performance of the scramjet engine can not be scaled photographically, full-scale tests with actual engine size are necessary. However, the ground test facilities for a high-Mach full-scale airframe-integrated test are usually unavailable due to the limitations of tunnel size and the large flow enthalpy. Data for complete airframe-integrated scramjets with close-to-flight conditions (matched pressure, temperature, velocity, and inflow composition) are generally rare in the literature. As a convenient yet accurate tool, CFD (Computational Fluid Dynamics) analyses are frequently employed for per-

* Corresponding author.
E-mail addresses: weiyao@imech.ac.cn (W. Yao), liuhang@imech.ac.cn (H. Liu), yuelj@imech.ac.cn (L. Xue), xiaoyabin@imech.ac.cn (Y. Xiao).

https://doi.org/10.1016/j.ast.2021.106941
1270-9638/© 2021 Elsevier Masson SAS. All rights reserved.

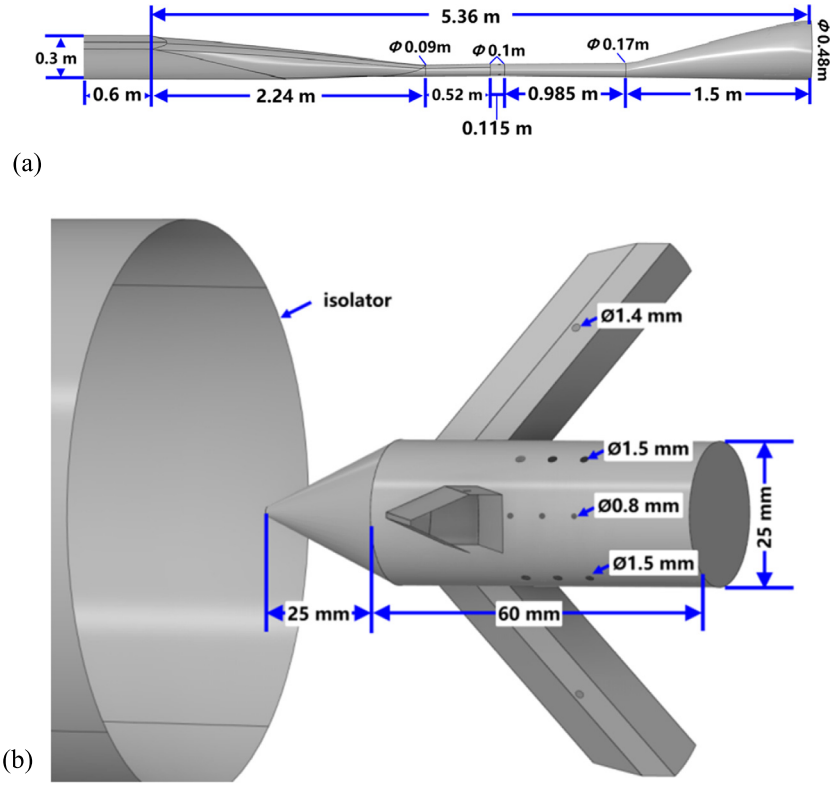

Fig. 1. Dimensions of (a) the scramjet with planner forebody and (b) the central strut.

formance optimization [8–11] as well as the understanding of underlying physical processes [12,13] in full-scale scramjet engines, e.g., the studies for flight Mach numbers of 8, 12, 13, and 15 [14,15]. Systematic CFD analyses are desired to build functional relationships between performance metrics (e.g., combustion efficiency and thrust) and scramjet operation conditions (e.g., flight Mach number, altitude, flowpath geometry) for the ultimate goal to minimize the drag while producing sufficient thrust. Marginal or optimistic results are expected from the parameter-performance study to determine the design criteria or examine the method feasibility.

Scramjets employing non-rectangular combustors have the potential to synchronically improve combustion stability and efficiency relative to those using planar geometries [16,17]. The reduced wetted area of non-rectangular combustors also lowers the viscous drag and the cooling requirements, which is especially important for high-Mach combustors with high dynamic pressure. The non-rectangular geometry can also raise the unstart limit caused by backpressure by removing the detrimental effect of corner flows in scramjet isolators and combustors, which can alternatively reduce isolator length. Free-jet testing of airframe integrated scramjets with rectangular-to-elliptical shape-transition (REST) inlet [18–22], elliptical combustor, and three-dimensional thrust nozzle in University of Queensland's T4 Reflected shock tunnel (RST) has shown the capability of delivering net thrust at speeds of Ma=7.5 [23], Ma=8 [24], Ma=8.7 [25], Ma=10 [26], and up to 12 [27–29]. The REST flowpath fueled by hydrogen was integrated with a forebody and streamlined external geometry to fully measure the force data at true-flight test conditions [30].

In order to better understand the sensitivities of engine performance to flight conditions, systematic evaluation of a full-scale high-Mach scramjet engine was numerically conducted in this study. The sensitivity of performance to flight Mach numbers from 7 to 10 and altitudes from 28 to 40 km are systematically analyzed by using high-fidelity large eddy simulation combined with a detailed chemical mechanism. The flow fields were also examined to reveal the combustion characteristics in a full-scale hypersonic combustor.

2. Physical models and numerical methods

2.1. Test case

The modeled geometry schematically shown in Fig. 1 has an entire length of 5.36 m. The planar forebody has a length of 0.6 m and is slightly broader than the inlet capture area. The 2.24-m-long inlet section extends from the leading edge of the body to the throat. The lip of the inlet sidewall turns inward and closes completely at 1.73 mm downstream of the inlet leading edge. The geometric contraction ratio of the inlet section is 10. The 0.52-m-long isolator section transits smoothly from the inlet into a round shape. The inlet end is close to a circle with a nominal diameter of 0.09 m, and the final isolator diameter is 0.1 m. The combustor consists of a 0.115-m-long constant-area round duct and a 0.985-m-long part diverging from 0.1 m to 0.17 m in diameter. The nozzle section is unilaterally expanded from 0.17 m to 0.48 m in diameter. All the scramjet components are aligned on the same horizontal plane with zero inclination angle.

The fuel is injected from a struct located inside the constant-area combustor section. There are a total of 24 injector portholes on the strut. Six portholes locate on each side of the pylons that connect the strut with the combustor wall at an angle of 53°. The other 18 portholes locate on the lateral surface of the strut, with each three in a row. The injectors in each row have a uniform interval of 5 mm. The rows of portholes behind the pylon have a smaller diameter of 0.8 mm, as a deep fuel penetration can be guaranteed when the jets are within the wake flow. The other ones have a diameter of 1.5 mm to enhance the penetration depth when injecting directly into the high-speed crossflow. All fuel jets are injected normally to the local wall tangential surface. The strut

Table 1
Summary of test flight conditions.

Airstream							Fuel (H_2) stream		
Y_{N2}: 0.767, Y_{O2}: 0.233							Y_{H2}: 1.0		
Ma	H (km)	T (K)	p (Pa)	U (m/s)	q (Pa)	Q_{air} (kg/s)	Q_{fuel} (kg/s)	Tt (K)	Ma
7	28	225	1616	2103	55434 (8)	2.95	0.086	298	1
7	30	227	1197	2112	41057 (4)	0.63	0.018		
8	30	227	1183	2415	53629 (7)	2.48	0.072		
8	33	231	767	2438	34374 (3)	1.66	0.048		
9	32	231	888	2742	50408 (6)	2.24	0.065		
9	37	242	433	2807	24564 (2)	1.06	0.031		
10	34	235	662	3076	46437 (5)	1.89	0.055		
10	40	250	287	3172	20099 (1)	0.79	0.023		

consists of a 25-mm-long 50°-angle cone and a 50-mm-long cylinder with a diameter of 25 mm. Similar strut and pylon structures [31–33] are frequently adopted in high-Mach scramjets to increase jet penetration into the core flow and enhance the mixing.

As summarized in Table 1, the scramjet was numerically tested for flight Mach numbers ranging from 7 to 10, with the altitudes from 28 to 40 km. The corresponding dynamic pressure varies from 20 to 55 kPa, and the stagnation temperature varies from 2100 to 4300 K. The mass capture of the air stream is resolved in the current modeling coupled both the internal and external flows and varies from case to case, while the fuel flow rate is automatically adjusted to maintain the global fuel equivalence ratio at 1.0.

2.2. Design of three-dimensional hypersonic inlet by stream-tracing technique

The hypersonic inlet is one of the critical components of a hypersonic scramjet to provide the required cycle temperature/pressure ratio in a wide operation range with the minimum aerodynamic loss (the highest total pressure recovery factor, or the minimum entropy increase). In order to obtain as high compression efficiency as possible, a streamline-tracked inlet based on Busemann base flow field [34] is adopted in this study. Busemann base flow field is an irrotational axisymmetric supersonic flow field. As shown in Fig. 1, all streamlines are isentropically contracted to the symmetric axis and finally transformed into a straight uniform flow parallel to the axis through a free-standing conical shock wave. This flow has high inviscid compression efficiency. The governing equation of Busemann flow is the Taylor MacColl equation,

$$-\frac{d^2V_r}{d\omega^2}\left[\frac{\gamma+1}{2}\left(\frac{dV_r}{d\omega}\right)^2 - \frac{\gamma-1}{2}(V_{max}^2 - V_r^2)\right] - \frac{\gamma-1}{2}\left(\frac{dV_r}{d\omega}\right)^3 cot\omega - \gamma V_r\left(\frac{dV_r}{d\omega}\right)^2 + \frac{\gamma-1}{2}(V_{max}^2 - V_r^2)\frac{dV_r}{d\omega}cot\omega + (\gamma-1)V_r(V_{max}^2 - V_r^2) = 0 \quad (1)$$

where ω is the angular coordinate of any point along the streamline in the axial coordinate system centering at the apex of the free-standing conical shock wave as in Fig. 1 (a), V_r is the radial velocity, Vmax is the velocity at which the total energy is converted into kinetic energy, and γ is the specific heat ratio. Eq. (1) is consistent with the equation describing supersonic conical flow but with different boundary conditions. The performance parameters of Busemann flow, such as pressure ratio, exit Mach number, temperature ratio, inviscid total pressure recovery factor, are entirely determined by the incoming Mach number and the angle of the conical shock wave. Therefore the performance requirements can be met by deliberately selecting these two values.

The design process of the hypersonic inlet can be divided into two steps. 1) The first step is to generate the inviscid inlet profile using the streamline tracing technique. Fig. 2 (a) shows the cross-section plane perpendicular to the symmetry axis of the Busemann flow field. The largest circle is the entrance boundary contour of the Busemann base flow field, and the smallest circle concentric with it is its exit boundary contour. The streamline tracing inviscid inlet profile is determined as the passing-through flow surface, which can be constructed for any closed curve drawn in a large circle. The area enclosed by the closed curve is the capture surface of the streamline tracing inlet. When the capture surface is circular, the resulting streamline tracing inlet shape is shown in Fig. 2 (b). As a subset of the Busemann base flow field, the flow field inside the streamline tracing inlet inherits all the latter's characteristics and has the same performance parameters. The capture ratio of the streamline tracing inlet is theoretically 100%. 2) The second step is the viscous correction. The development of the boundary layer insider the inlet will gradually occupy the flow path of the core flow. The viscous interaction will make the core flow lose the good characteristics originally designed. Viscous correction is to expand the wall outward by a certain distance to restore the designed characteristics of the core flow. In this study, the displacement thickness of the boundary layer is estimated by the reference temperature method [34], and the inlet wall is expanded at this thickness along the normal direction of the inlet surface.

2.3. Governing equations with dynamic zone flamelet model (DZFM)

The unsteady and three-dimensional Favre-averaged compressible reactive Navier-Stokes equations (rNSE) are solved for a set of conservative variables ($\overline{\rho}$, $\tilde{u}_i$, $\tilde{H}_t$, $\tilde{\xi}$, Q_α) [35,36],

$$\frac{\partial\overline{\rho}}{\partial t} + \frac{\partial\overline{\rho}\tilde{u}_j}{\partial x_j} = 0 \quad (2)$$

$$\frac{\partial\overline{\rho}\tilde{u}_i}{\partial t} + \frac{\partial\overline{\rho}\tilde{u}_j\tilde{u}_i}{\partial x_j} + \frac{\partial\overline{p}}{\partial x_i} - \frac{\partial\tilde{\tau}_{ij}}{\partial x_j} = -\frac{\partial\tau_{ij}}{\partial x_j} \quad (3)$$

$$\frac{\partial\overline{\rho}\tilde{H}_t}{\partial t} + \frac{\partial\overline{\rho}\tilde{u}_j\tilde{H}_t}{\partial x_j} - \frac{\partial}{\partial x_j}\left(\overline{\rho}D_T\frac{\partial\tilde{H}_t}{\partial x_j} + \sum_{\alpha=1}^{L}\overline{\rho}D_\alpha\frac{\partial\tilde{Y}_\alpha}{\partial x_j}\tilde{H}_\alpha\right) - \frac{\partial\overline{p}}{\partial t} - \frac{\partial\tilde{u}_j\tilde{\tau}_{ij}}{\partial x_j} = -\frac{\partial\Psi_{T,j}}{\partial x_j} \quad (4)$$

$$\frac{\partial\overline{\rho}\tilde{\xi}}{\partial t} + \frac{\partial\overline{\rho}\tilde{u}_j\tilde{\xi}}{\partial x_j} - \frac{\partial}{\partial x_j}\left(\overline{\rho}D_\alpha\frac{\partial\tilde{\xi}}{\partial x_j}\right) = -\frac{\partial\Psi_{\xi,j}}{\partial x_j} \quad (5)$$

$$\widetilde{\xi''^2} = C_{var}\Delta_{sgs}^2\left|\nabla\tilde{\xi}\right|^2 \quad (6)$$

$$\rho_\eta\frac{\partial Q_\alpha}{\partial t} + \langle\rho u_j|\eta\rangle_{zone}\frac{\partial Q_\alpha}{\partial x_j}$$

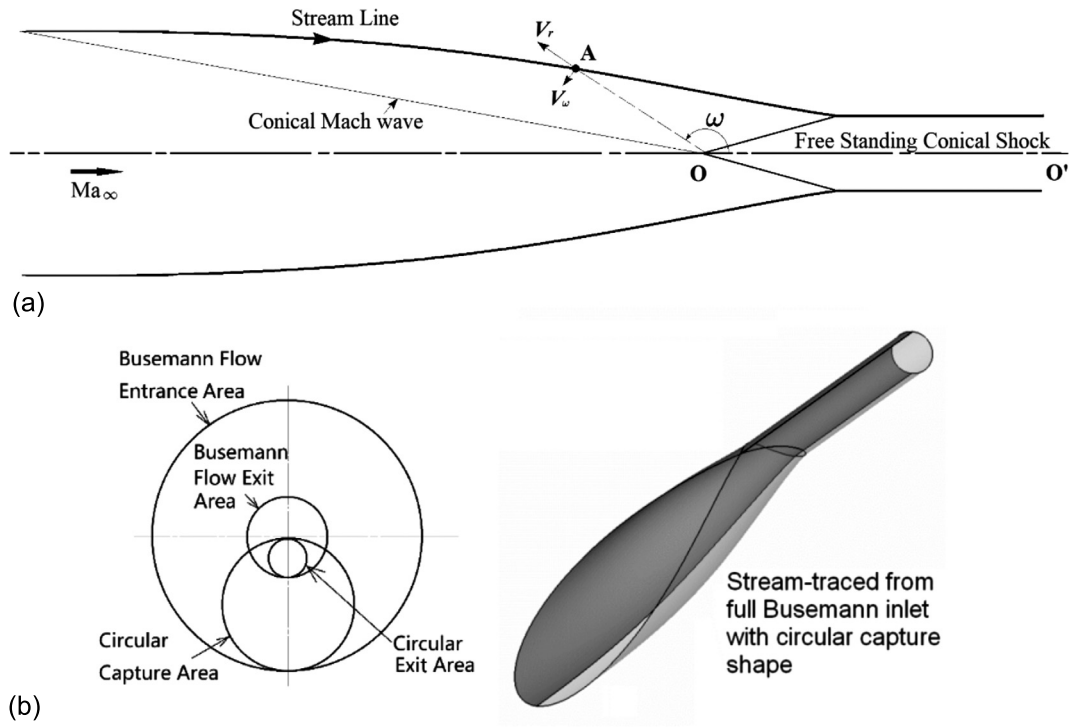

Fig. 2. (a) Busemann base flow, (b) design schematic of the hypersonic inlet.

$$= \rho_\eta \frac{D_\alpha}{D_\xi} \langle \chi | \eta \rangle_{zone} \frac{\partial^2 Q_\alpha}{\partial \eta^2} + \rho_\eta \left(\frac{D_\alpha}{D_\xi} - 1 \right) M_\eta \frac{\partial Q_\alpha}{\partial \eta} + \rho_\eta \langle W_\alpha | \eta \rangle \quad (7)$$

$$\overline{p} = \overline{\rho} R \tilde{T} \quad (8)$$

$$\tilde{H}_t = \tilde{H} + \frac{1}{2}\tilde{u}_i\tilde{u}_i = \tilde{H}^0 + \int_0^T C_p dT + \frac{1}{2}\tilde{u}_i\tilde{u}_i \quad (9)$$

Here the bar "-" and the tilde "∼" represent averaged and Favre-averaged quantities respectively, the subscript *zone* denotes an averaged value with a zone, t denotes the time, x_i is the Cartesian coordinate in direction i, $\overline{\rho}$ is the mean density, u_i and $\tilde{u}_i$ are the velocity component in the x_i direction (spatial dimension $i = 1, 2, 3$), $\overline{p}$ is the mean pressure, $\tilde{\tau}_{ij}$ is the viscous stress tensor, $\tilde{H}_t = \tilde{H} + 0.5\tilde{u}_i^2$ is the total absolute enthalpy obtained as the sum of the absolute enthalpy $\tilde{H}$ and the resolved kinetic energy, the absolute enthalpy $\tilde{H}$ is calculated as the sum of the formation enthalpy $\tilde{H}^0$ at standard reference state and the sensible enthalpy change from the reference temperature to T; $\tilde{\xi}$ and $\widetilde{\xi''^2}$ are the mean mixture fraction and its variance, C_{var}=0.1 [37] and Δ_{sgs} is the filter width for subgrid turbulence; $Q_i = \langle Y_\alpha | \xi(x,t) = \eta, x \in zone \rangle$ is the conditionally-averaged mass fraction Y_α for species α within a zone, χ is the scalar dissipation rate defined as $\chi = D(\nabla\xi)^2$, $\rho_\eta = \langle \rho | \eta \rangle$, conditional diffusion $M_\eta = \langle \nabla \cdot (\rho D_\xi \nabla \xi) | \eta \rangle_{zone}$, and $\langle W_\alpha | \eta \rangle$ is the conditional mass production rate of chemical species α in the unit of s^{-1}; D_α is mixture-averaged mass diffusivity of species α, D_ξ represents the mean mixture diffusivity, D_T is the thermal diffusivity, $\tilde{T}$ is the temperature; $R = R_u/W$ is the gas constant, $R_u = 8.314\ J \cdot mol^{-1} \cdot K^{-1}$ is the universal gas constant, $W = \left(\sum_{\alpha=1}^{L} Y_\alpha / W_\alpha \right)^{-1}$ is the molar weight of the multicomponent mixture; The thermodiffusion (Soret effect), barodiffusion, and mass-driven diffusion of heat (Dufour effect), SGS species diffusive flux, SGS energy diffusive flux, SGS viscous dissipation are ignored in Eqs. (4)–(5) [35].

The turbulent combustion is decoupled from the flow modeling by using Dynamic zone flamelet model (DZFM) [38]. In DZFM, the zone flamelet equation (6) is solved instead of the mean species transport equation. The mean species mass fractions $\tilde{Y}_\alpha$ are obtained from the flamelet variable Q_α by probability density function (PDF) weighted integration,

$$\tilde{Y}_i = \int Q_\alpha P(\eta) d\eta \quad (10)$$

where $P(\eta)$ is the β-function of the mean mixture fraction $\tilde{\xi}$ and its variance $\widetilde{\xi''^2}$. Following Eq. (7), such a concept of solving the transport of conditional variables in four-dimensional space (three-dimensional space together with one-dimensional mixture fraction space) has been adopted in the Conditional Moment Closure (CMC) model [39]. However, in DZFM, the valid zone for each flamelet, which is represented by a set of conditional variables, is defined by the local flow variable(s) (e.g., mixture fraction in this study). Thus the flamelet zone will be constantly reshaped with the time-variation of mixture fraction distribution to characterize the local turbulence-chemistry interaction better as similar reacting statuses have been assembled to the same zone. A recent study [38] has shown that an improved statistical homogeneity of conditional variables can be achieved by using such a dynamic zone method.

In supersonic flow, both the density and velocity distributions are primarily influenced by the flow compressibility and discontinuities, and it is hard to correlate them with the mixture fraction. Instead of constructing separate models for ρ_η and $\langle \overrightarrow{U} | \eta \rangle$, the concept of conditional mass flux $\langle \rho \overrightarrow{U} | \eta \rangle$ is introduced as it can keep consistency even when across the shock discontinuities. It is assumed that the conditional mass flux is conserved with the mean value; thus a simple mean model is used in this study with $\langle \rho \overrightarrow{U} | \eta \rangle = \overline{\rho} \overrightarrow{U}$. The conditional scalar dissipation rate $\langle \chi | \eta \rangle$ is modeled by amplitude mapping closure (AMC) model [40] for its simplicity and robustness, since no significant difference has been

observed among AMC [40], Girimaji [41], and PDF integration [42] models for conditional scalar dissipation rate [43].

In order to estimate the conditional reaction rate in the mixture fraction space, i.e., $\langle W_\alpha|\eta\rangle$ in Eq. (7), the conditional temperature is needed. In the current implementation, the conditional energy equation is not solved, and the temperature in the physical space needs be mapped to that one in the mixture fraction space. It is usually reasonable to ignore the enthalpy fluctuations ($H' \sim o(0)$) [44], and therefore the corresponding PDF distribution of $\langle H|\eta\rangle$ can be assumed to be a Dirac delta function centered on the local mean value of the enthalpy $\tilde{H}$. Then $\langle H|\eta\rangle$ can be estimated using an approach of historical statistics by integrating over all CFD cells within a single flamelet zone [45],

$$\langle H|\eta\rangle = \frac{\int_{zone}\left\langle \tilde{H}|\tilde{\xi}=\eta\right\rangle \overline{\rho}P(\eta)\,dV}{\int_{zone}\overline{\rho}P(\eta)\,dV} \tag{11}$$

Such a statistical approach is especially suitable for high-resolution LES because a flamelet zone can contain sufficient CFD cells to give a good approximation to the actual conditional mean. The statistical enthalpy approach mimics the enthalpy defect/excess model [46,47] but provides a more reasonable estimation of the enthalpy defect/excess status in each zone. Then, the conditional temperature can be calculated as a function of conditional enthalpy and conditional mass fractions $Q_T = f(\langle H|\eta\rangle, Q_\alpha)$. The current historical statistics approach also significantly saves the computational cost in solving the conditional energy equation with complex yet undetermined conditional source terms.

According to the Stokes' hypothesis, which ignores the bulk viscosity, the shear-stress tensor for a Newtonian fluid is calculated as,

$$\tilde{\tau}_{ij} = \overline{\rho}\nu\left(\tilde{T}\right)\left(2\tilde{S}_{ij} - \frac{2}{3}\delta_{ij}\tilde{S}_{kk}\right) \tag{12}$$

where ν is a temperature-dependent kinetic viscosity, and the strain-rate tensor of the resolved scales is calculated as:

$$\tilde{S}_{ij} = \frac{1}{2}\left(\frac{\partial\tilde{u}_i}{\partial x_j} + \frac{\partial\tilde{u}_j}{\partial x_i}\right) \tag{13}$$

The Reynolds stress defined as $\tau_{ij} = \overline{\rho}\left(\widetilde{u_i u_j} - \tilde{u}_i\tilde{u}_j\right)$ is modeled by the Boussinesq eddy viscosity hypothesis, where the Reynolds stresses are also taken to be proportional to $\tilde{S}_{ij}$,

$$\tau_{ij} = \underbrace{\left(\tau_{ij} - \frac{1}{3}\delta_{ij}\tau_{kk}\right)}_{\text{deviatoric}} + \underbrace{\frac{1}{3}\delta_{ij}\tau_{kk}}_{\text{isotropic}} = -\overline{\rho}\nu_{sgs}\left(2\tilde{S}_{ij} - \frac{2}{3}\delta_{ij}\tilde{S}_{kk}\right) + \frac{2}{3}\delta_{ij}k_{sgs} \tag{14}$$

Here ν_{sgs} is the subgrid-scale (SGS) eddy viscosity given by a specified turbulence model that will be described in the following section, k_{sgs} is the unresolved SGS turbulent kinetic energy.

The turbulent enthalpy flux term $\Psi_{T,j} = \overline{\rho}\left(\widetilde{u_j H_t} - \tilde{u}_j\tilde{H}_t\right)$ is modeled by the gradient diffusion assumption as

$$\Psi_{T,j} = -2\overline{\rho}\frac{\nu_{sgs}}{Pr_t}\frac{\partial\tilde{H}_t}{\partial x_j} \tag{15}$$

where Pr_t is the turbulent Prandtl number. The turbulent species diffusion term $\Psi_{\alpha,j} = \overline{\rho}\left(\widetilde{u_j Y_\alpha} - \tilde{u}_j\tilde{Y}_\alpha\right)$ is also modeled using the gradient diffusion assumption as

$$\Psi_{\alpha,j} = -2\overline{\rho}\frac{\nu_{sgs}}{Sc_t}\frac{\partial\tilde{Y}_\alpha}{\partial x_j} \tag{16}$$

where Sc_t is the turbulent Schmidt number. The turbulent Prandtl and Schmidt numbers are proportional to the square root of the reciprocal of the species and enthalpy fluctuations. Although it is reported that the results are influenced by the choice of proper Prandtl and Schmidt numbers in RANS modelings [48–50], less influence is observed for LES modelings of hypersonic combustion, probably because the diffusion time scale is much larger than the convection one [51], as well as that most of the mixing and heat transfer behavior has been directly resolved. In this study, unity Prandtl and Schmidt numbers are assumed.

2.4. Physical models and solver details

The turbulence closure is modeled by Improved Delayed Detached Eddy Simulation (IDDES) [52] based on the background RANS model one-equation Spalart–Allmaras model [53]. In IDDES, the turbulent viscosity in the boundary layer is modeled by the RANS mode to alleviate the computational cost, while the LES mode resolves the internal domain. In IDDES, the near-wall region is resolved by traditional RANS modeling, and the outer flow region is treated with LES. The governing equations for RANS and LES are formally similar, except that the subgrid-scale viscosity (ν_{sgs}) in LES is replaced by a turbulent viscosity (ν_t) in RANS. As what improves over the traditional DES (Detached Eddy Simulation) model, the IDDES length scale is determined by both the local cell sizes and the off-wall distance, and a shielding function is used to provide a smooth transition between the boundary layer and the outer flow regions, in order to restore the balance between the modeled Reynolds stresses and the resolved stresses [54]. The IDDES length scale Δ_{IDDES} is served as the local filter width of subgrid turbulence for both the RANS and LES regions in calculating the mean scalar dissipation rate $\tilde{\chi}$ [55,56],

$$\tilde{\chi} = \underbrace{D_\xi\left|\nabla\tilde{\xi}\right|^2}_{resolved} + \underbrace{\frac{\nu_{sgs}}{Sc_t}\left|\nabla\tilde{\xi}\right|^2}_{subgrid} = \underbrace{D_\xi\left|\nabla\tilde{\xi}\right|^2}_{resolved} + \underbrace{\frac{\nu_{sgs}}{Sc_t}\frac{\widetilde{\xi''^2}}{C_{var}\Delta_{IDDES}^2}}_{subgrid} \tag{17}$$

where both resolved and sub-grid contributions are included to account for the different turbulence-resolving levels caused by adaptive modeling strategies (e.g., RANS and LES modes) as well as varying mesh resolutions. Scalar dissipation rate describes the local effect of molecular mixing on chemistry and bridges the interplay between turbulence and combustion. As shown in Eq. (7), the main influence of turbulence exerting on the reactions in the mixture fraction space is through the conditional scalar dissipation rate, which constantly diffuses the conditional species and may lead to extinction under extreme values. The scalar dissipation rate is proportional to the scalar gradient, implying that a steeper gradient will produce a denser flamelet zone division based on mixture fraction, which would be beneficial for homogenizing the local turbulence effect. The conditional scalar dissipation rate is calculated by the amplitude mapping closure (AMC) model [40],

$$\langle\chi|\eta\rangle_{zone} = \frac{1}{2}\tilde{\chi}\frac{G(\eta)}{\int G(\eta)P(\eta)\,d\eta} \tag{18}$$

with $G(\eta) = e^{-2\left[erf^{-1}(2\eta-1)\right]^2}$.

The turbulence-chemistry interaction is accounted for by the DZFM model [57] [38,58], which divides the domain into a finite number of zones and applies a local flamelet for each one. In addition to the spatial coordinates used to define the coarser CMC grids in the traditional CMC implementation [45], the flow field is also used in DZFM to define the flamelet zone. Only the streamwise coordinate is used to delimit the zones from the upstream

ones to the downstream ones in a manner consistent with the evolution of reaction progress. Since the convection transport is solved in Eq. (7), the downstream zones can succeed the reacting status from their upstream counterparts, which is the physical picture describing the inheritance relationship between unburnt flamelet, burning flamelet, and burnt flamelet. After cutting the streamwise flow into different stumps, a further refinement of the zones can be performed based on the similarity of local turbulent reacting statuses. Different combinations of flow indices, such as mixture fraction, pressure, temperature, significant species compositions, or reaction progress variable, can be adopted to regroup the CFD cells into different flamelet zones. Taking advantage of the clustered cells, the conditionally-averaged thermochemical properties of the cell cluster are then used to represent and evolve the combustion chemistry within each zone, improving the computation efficiency as the direct integration cell by cell is avoided. In this study, the domain is firstly spatially cut into 234 zones in the streamwise direction, and then each stump zone is further divided into 91 annual zones according to the local mixture fraction, resembling the annual tree rings on a stump. A sensitivity analysis [38] shows that the 91 division in the mixture fraction space can accurately identify the reacting statuses while does not significantly increase the computational burden. The division in the mixture fraction space clusters more around the stoichiometric value, while the cutting in the spatial domain is uniform. Both the zone division and the flamelets are constantly and dynamically updated with the flow evolution to better represent the local reacting status and diminishes the redistribution effect of conditional variances. When updating the zone division, the flamelet is updated through a mass-weighted average of the old conditional variables $\langle\phi|\eta\rangle_{old}$ over all CFD cells within the new zone,

$$\langle\phi|\eta\rangle = \frac{\int_{new\ zone} \overline{\rho}\,\langle\phi|\eta\rangle_{old}\, dV}{\int_{new\ zone} \overline{\rho} dV} \tag{19}$$

Due to the compression/expansion waves, shock waves, and strong viscous heating, large variations in the total enthalpy and pressure exist in compressible flows, which introduces additional degrees of freedom in the manifold representing the thermochemical state and makes the tabulation of flamelet extremely challengable. At least two additional factors, i.e., pressure and enthalpy, need to be added to the state space for mixture composition to form the so-called compressible extended flamelet table (CEFT) [59,60]. In DZFM, the influence of local pressure and enthalpy level has been considered in the evolution of each zone flamelet. The tabulation of temperature in flamelet-like models is even more difficult than the tabulation of species as significant enthalpy excess/defect may be caused by the flow compressibility. The temperature is no longer given by a chemistry table but iteratively computed given the mixture composition and the total energy, which is resolved by incorporating kinetic energy exchange, pressure work, viscous heating to account for the compressibility effects in supersonic flows [59,61–65]. The same temperature inference method is adopted in the implementation of DZFM. In transported PDF models [66] and Multiple Mapping Conditioning (MMC) model [67], the compressibility effects of kinetic energy exchange, pressure work, and viscous heating can be incorporated into the stochastic energy equation when modeling compressible flows.

The combustion chemistry is resolved by the mechanism of Jachimowski [68] with 13 species and 33 reactions, which has been extensively validated in previous supersonic combustion modelings [21,27,69]. The thermodynamic and transport properties of the gas mixture, such as absolute enthalpy, specific heat, thermal conductivity, viscosity, thermal and mass diffusivities, are calculated using the chemical kinetics package CHEMKIN-II [70] based on the JANAF (Joint Army-Navy-Air Force)-format thermochemical database [71] and a CHEMKIN-format transport database. The viscosity, specific heat, and conductivity are all assumed independent of pressure and only depend on temperature. The mixture-averaged viscosity and thermal conductivity are calculated using the modified Wilke's law [72] and the combination averaging, respectively. The mixture thermal diffusivity is then calculated based on the conductive and specific heat. Mixture-averaged mass diffusivities are used, and the mass conservation is achieved by setting the nitrogen as the inert gas, whose mass fraction is computed by subtracting the sum of the remaining mass fractions from unity.

The computation is performed by an OpenFOAM [73] based compressible reacting flow solver Amber (formerly known as AstroFoam), which adopts the low-dissipative hybrid scheme [74] combining the dissipative KNP scheme [75] with the nondissipative central scheme [76]. Amber is developed from the non-reacting rhoCentralFoam and has been extensively validated in supersonic non-reacting flow [38,77–85] and combustion cases [17,38,51,86–90]. Similar density-based solver based on rhoCentralFoam has been developed for different purposes, e.g., two-phase reacting flow [91,92], magnetohydrodynamics [93], and aerodynamic analysis [94], showing the robustness and accuracy of the basic flow solver based on the central-upwind KT/KNP scheme [79].

The domain is meshed by the combination of tetrahedral cells in 94.8 vol%, wedge cells in 5.1 vol%, and pyramid cells in 0.1 vol% near the corners to accommodate the complex struct geometry inside the flowpath. A total of 104.77 million unstructured cells were applied with a denser distribution clustering around the injectors. The maximum cell size is 0.8 mm, and the minimum size around the injectors is 75 μm. A near-wall inflation layer with 15 prism layers and a total thickness of 1 mm is attached to the chamber wall to ensure that the first near-wall cell is located in a nondimensional wall distance $y^*<1$. In the final mesh, 94.7% of the domain is meshed by tetrahedral cells, 5.2 vol% by wedge cells, and the rest by pyramid cells. Mesh quantity analysis shows that cells in 99.5% of the domain volume have skewness less than 0.5, and cells in 99.4% of the domain volume have orthogonal quality larger than 0.5. Grid sensitivity analysis was conducted for meshes with 54.13 million, 71.76 million, 104.77 million, and 125.10 million cells. As shown in Fig. 3, the mean relative errors with the finest mesh (125.10M) are as small as 1.7%, 1.2%, and 0.8% from the coarsest to the secondary finest meshes. The linear descent trend for the mean relative errors indicates that grid independence has been achieved. The following analysis and discussion are all based on the secondary finest mesh (104.77M) to better resolve the coherent flow structures while alleviating the huge computational cost.

The current modeling framework, including the physical models and numerical methods, was firstly validated in the University of Queensland (UQ)'s REST scramjet [28]. The modeled REST scramjet operates at a flight Mach number of 12 and an altitude of 36 km. The domain contains a similar inlet part of the planar forebody, a similar inward-turning inlet blending a rectangular capture area to an elliptical combustor, and a conic nozzle. As shown in Fig. 4, the wall pressure was well captured by the current modeling framework with 92.52 million cells in comparison with the measurement and the UQ prediction with 45 million cells, with important features like the double peak were reproduced. Details of the validation can be found in [95].

3. Results and discussion

Fig. 5 shows the quasi-steady temperature fields under different dynamic pressures. With the increasing dynamic pressure, the

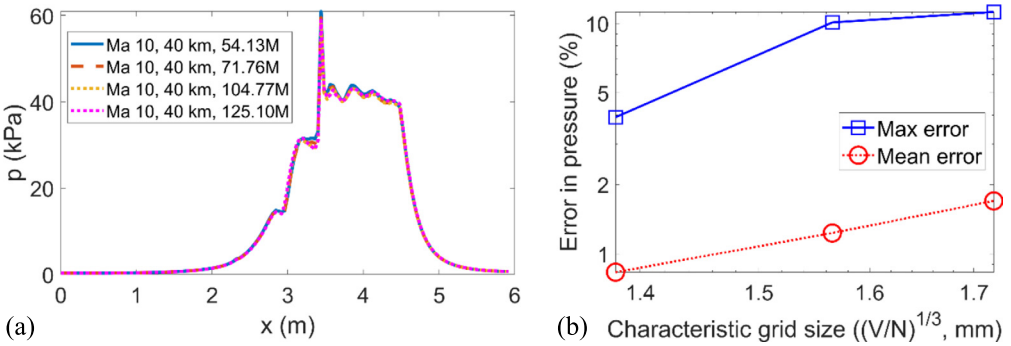

Fig. 3. Grid sensitivity of mesh resolutions, (a) pressure profiles, (b) relative errors in log-log coordinate.

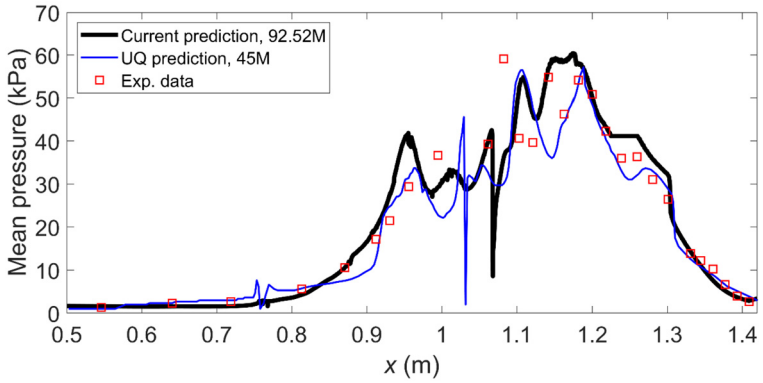

Fig. 4. Pressure validation of current modeling framework for REST scramjet [28].

initial shock wave moves upstream as the backpressure in the combustor increases. From all the cases, inlet unstart occurs for the lowest flight Mach of 7 at 30 km, whose dynamic pressure is not the lowest one. Clear temperature stratification in the thrust nozzle can be observed, and the existence of massive OH radicals indicates that the combustion reactions are far from equilibrium till the nozzle exit. Combustion occurs in both the downstream and upstream of the strut, and the visible flame length in the upstream increases as more fuel is propagated reversely. For the upstream combustion, the flame is more attached to the upper wall. More intense combustion occurs downstream of the strut for Mach 9 at 32 km and Mach 10 at 34 km, whose dynamic pressure is in the middle of all the cases and among 45-50 kPa. It is observed that only the hydrogen injected from the pylon connected to the upper wall propagates upstream, while hydrogen from the other two pylons always moves downstream. This is because the boundary layer separation is more prone to occur in the upper wall when impinged by the incident shock wave. The upstream propagated hydrogen is auto-ignited by the oblique shock train and then aids the downstream combustion through preheating the inflow and radical farming. The downstream flame appears as a thin layer following the jet wakes, indicating that the transverse mixing is slow under the crossflow Mach number close to 3, even with the aids of the pylon and strut mixers.

Fig. 6 shows the near-field flow structures and variable fields around the strut for the case with Mach 10 and 40 km. As observed in Fig. 6 (a), the Mach barrels formed by the fuel jet issued from the 1.4-mm-diameter and 1.5-mm-diameter injectors are obviously larger than the 0.8-mm-diameter ones. The hot horseshoe vortex can be clearly identified from the cold fuel jet, whose Mach barrels and Mach disks can also be outlined in the numerical schlieren. The attached shock wave formed on the blunt cone nose of the strut intersects with the reacting layer in the upstream recirculation zone on the upper side while intersects with the boundary layer and causes the separation in the lower side. The reflected shock wave originated from the separated bubble further intersects with the fuel stream and aids the ignition. The burning mixing layer can be identified in the numerical schlieren as it has a significantly lower density than the surrounding cold air. From the streamlines in Fig. 6 (b), four main recirculation zones can be identified before and behind the pylon, behind the strut, and inside the separation bubble, respectively. The first three recirculation zones can be classified as the spanwise roller formed by the blocking effect of solid wall and act the role of the passive mixer through entraining fuel into the upstream and the crossflow. The observation that the streamlines inside the separation bubble do not close on the clip plane implies that the recirculation zone exhibits more three-dimensional characteristics. The volume expansion due to intense combustion near the upper wall, as indicated by the high temperature in Fig. 5 (a), drives the flow streamlines away from the wall and towards the internal flow in the downstream after the strut. As expected, the engine runs in scramjet mode, with a shrunk supersonic throat between the strut and the separated bubble. Before the strut, the displacement effect of the subsonic upstream recirculation zone reduces the flow speed in the supersonic core from Ma>5 to below 5. Although most of the intense combustion occurs under the subsonic condition, there is combustion region overlap with supersonic regions. Different from the sonic detonation-driven combustion [96], where the mixture is initially premixed and subsonic, the hypersonic combustion occurs initially under the nonpremixed yet hypersonic condition. The premixed region denoted by TFI>0 attains supersonic (Ma>1) or even hypersonic (Ma>5) speed after the momentum exchange; thus there is no barrier for the burning mixture to cross the sonic line. The formation of the premixed mixture (denoted by TFI>0 in Fig. 6 (d)) shortly after the fuel injection suggests that the mixing is adequate due to the recirculation zones induced by the strut and pylon, although with the pay in total pressure loss. Judging from the flame lift-off distance in the streamwise direction, the premixed or partially-premixed regions

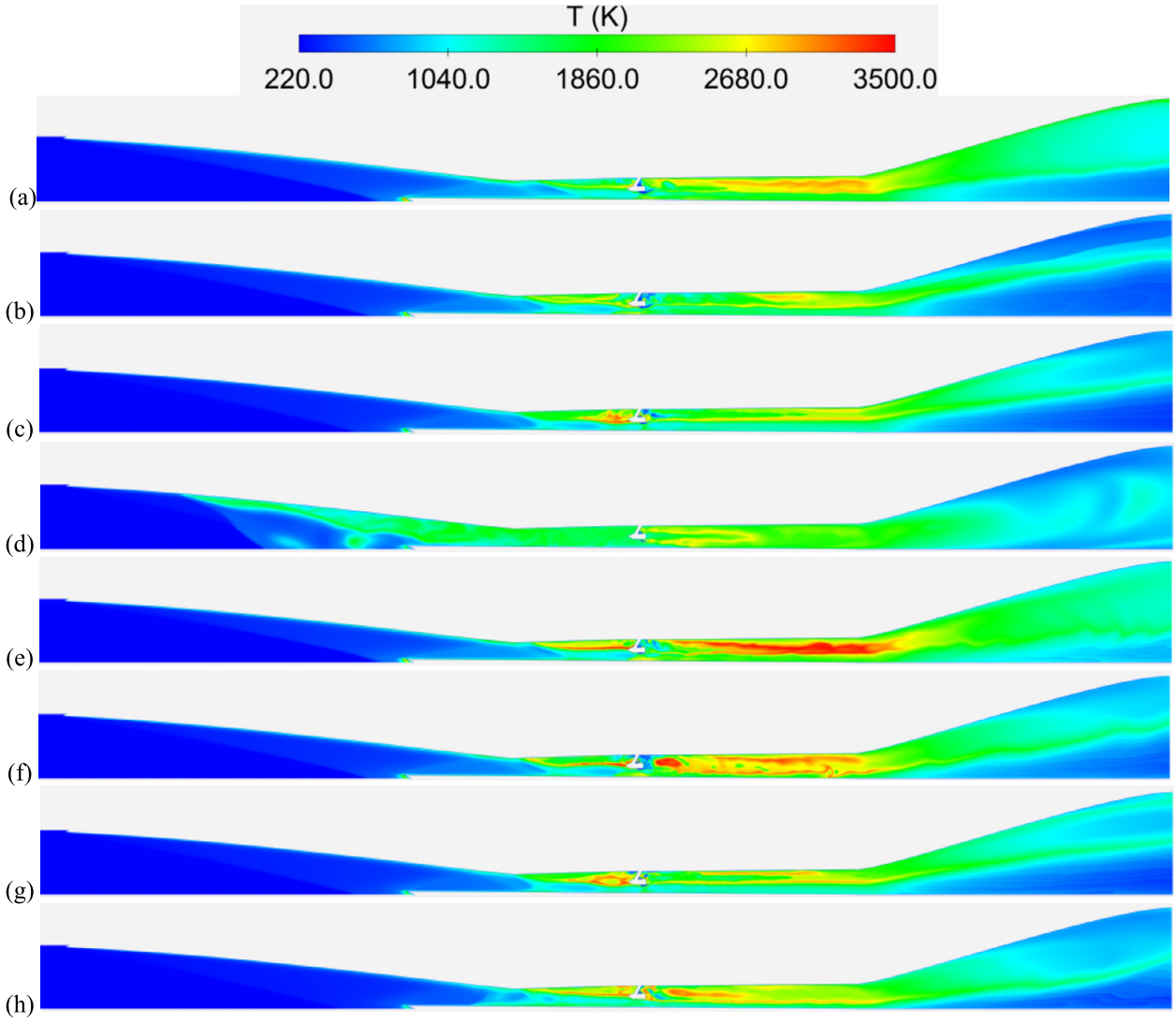

Fig. 5. Contours of static temperature under different dynamic pressures, the subfigures are sorted in ascending order of dynamic pressure: (a) Mach 10 at 40 km, (b) Mach 9 at 37 km, (c) Mach 8 at 33 km, (d) Mach 7 at 30 km, (e) Mach 10 at 34 km, (f) Mach 9 at 32 km, (g) Mach 8 at 30 km, (h) Mach 7 at 28 km. (For interpretation of the colors in the figure(s), the reader is referred to the web version of this article.)

effectively aid the combustion and stabilize the flame. Chemical Explosives Mode Analysis (CEMA) index, which is defined as the maximum absolute eigenvalue of the chemical source-term Jacobian matrix, can be used to identify the transient ignition region with CEMA>0 s^{-1} and post-ignition and diffusion-controlled regions with CEMA<0 s^{-1}. Fig. 6 (e) shows the signed log-scaling of the CEMA variable, $\text{sign(CEMA)} \times \log_{10}(1 + |\text{CEMA}|)$, where a minimum of 1 s^{-1} is added to filter out the chemically inactive zone with $|\text{CEMA}| < 1$. There is no apparent violent ignition region, and most of the combustion is chemically slow and diffusion-dominated as the residence time in hypersonic flow is too short to allow a local completion of full ignition chain reactions. The upstream recirculation zone and the post-strut regions with temperature higher than 2000 K have the highest reaction rate with $|\text{CEMA}| > 10^8$ s^{-1}, the rest region with fuel addition in the combustor has a lower reaction rate of $|\text{CEMA}| \sim 10^6$ s^{-1}, while the pure air crossflow region still has a nonnegligible reaction rate of $|\text{CEMA}| \sim 10^4$ s^{-1} because the dissociation reactions of N_2 and O_2 have been included.

In Fig. 7 (a), the peak of section-averaged pressure generally increases with the increase of dynamic pressure as more air can be captured while the global fuel equivalence ratio is maintained at unity. The continuous pressure rise is before x=2.84 m is due to the compression by the inward-turning inlet. After xs=2.84 m, the pressure reaches a plateau and peaks at the struct location of x=3.36 m. A sudden pressure drop occurs at the start of the nozzle. Before the strut, the pressure increases with pressure except that the pressure of Mach 10 at 34 km should be lower than the pressure of Mach 8 at 33 km. This abnormality can be due to the more concentrated heat addition (a narrow reaction zone in Fig. 5 (c)) before the strut. After the strut, the pressure varies exactly in the same order as the dynamic pressure of the inlet.

The peak wall heat flux was present in Fig. 7 (b). There are two major peaks located at x=0.72 m and 3.44 m, corresponding to the leading edge of the inlet and the strut, respectively. The wall heat load by the combustion at the strut is found to be smaller than the aerodynamic heating at the inlet edges. In the inlet section before x=2.4 mm, there are a series of high heat flux peaks of a similar order of magnitude with the heat load at the strut imposed by the combustion. Those high heat fluxes are mainly located at the leading edge notch, which has a thickness of 2 cm. The intense aerodynamic heating at the leading edge suggests that special thermal protection must be adopted to prevent it from deformation or damage, as the initial compression by the leading

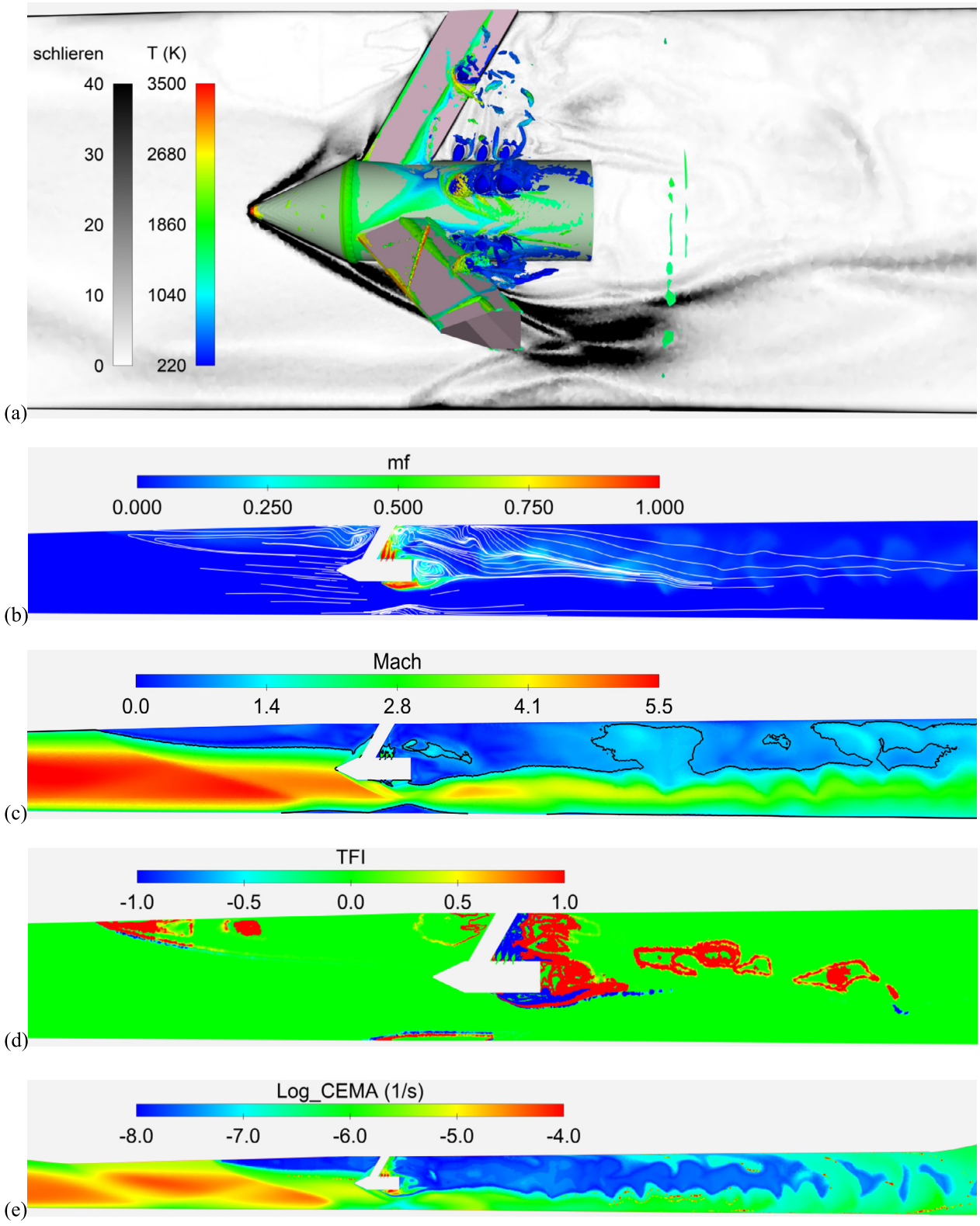

Fig. 6. Close views of (b) near-field vortex structure on schlieren background, (b) mixture fraction distribution with streamlines, (c) contours of Mach number delimited by sonic line, (d) Takeno Flame Index (TFI) [97], and (e)) signed log-scaling of CEMA [98].

edge shock is essential for the inlet mass capture. A secondary peak can be observed in the isolator section between x=3 m and 3.16 m, which are due to the upstream propagation of combustion shown in Fig. 5. The wall heat flux was calculated by fixing the wall temperature to 300 K. Extremely high peak heat flux close to 60 MW (Ma 10 at 40 km) caused by aerodynamic heating was observed at the leading edge, while high peak flux close to 40 MW (Mach 10 at 34 km) was caused by the combustion around the strut. The wall heat flux has an average value of around 5 MW in the combustor and reduces to below 2 MW in the nozzle section. Therefore, special thermal protection should be given to the inlet and combustor sections.

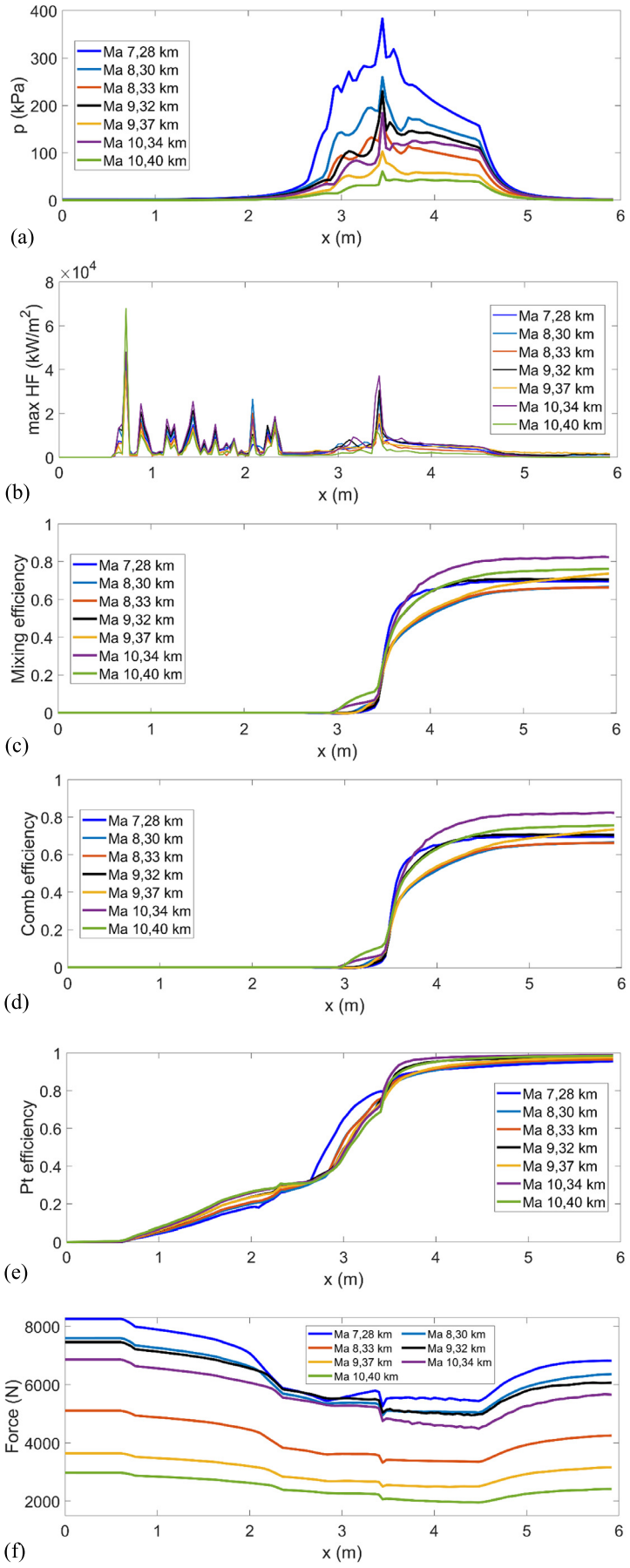

Fig. 7. (a) Static pressure, (b) peak heat flux, (c) mixing efficiency, (d) combustion efficiency, (e) total pressure loss coefficient, and (f) streamwise thrust.

From Fig. 7 (d), the initial rise in combustion efficiency before the strut confirms the upstream propagated combustion shown in Fig. 5. The combustion efficiency does not have an apparent dependence on dynamic pressure but is influenced more by the flight Mach number. The combustion efficiency profiles are highly similar to the mixture efficiency profiles in Fig. 7 (c), suggesting the rule of mixed is burnt in high enthalpy flow. The two cases at Mach 10 have the highest final combustion efficiencies, i.e., 82% and 75% for 34 km and 40 km, respectively. At Mach 7 and 9, the final combustion efficiency is higher than 70%. While at Mach 8, the final combustion efficiency is only 66%. From the combustion profiles, most of the fuel consumption is consumed before 70 cm after the strut. The combustion reactions approach equilibrium towards the nozzle exit except for Ma 9 at 37 km, where a longer flowpath is required to achieve a higher combustion efficiency.

The total pressure loss in Fig. 7 (e) is produced since the flow entering the cowl of the inlet and reaches around 70% before the strut. The total pressure loss can be generally divided into three stages: shock-wave-induced from the inlet leading edge at x=0.6 m to the cowl notch at x=2.64 m, shock-wave and friction-induced from the cowl notch to the strut at x=3.4 m, and momentum-exchange and heat-addition-induced after the strut. In the second stage, the case of Mach 7 at 28 km has a higher total pressure loss due to the stronger pseudo shock train caused by the higher back-pressure. A drastic loss was induced within 20 cm since the strut. The final loss approaches 96-99%, which implies a nearly two-fold entropy increase of $2C_v\,(\gamma-1)$, where γ is the heat capacity ratio and C_v is the volumetric specific heat. Remembering that scramjets operating below Mach 8 usually have a total pressure loss below 80% [51,90], how to alleviate the total pressure loss is especially important for high-Mach scramjets.

In Fig. 7 (f), the stream force function defined as the summation of pressure force and momentum flux $\mathrm{I} = \mathrm{pA} + \rho \mathrm{u}^2\mathrm{A}$ (A is the cross-section area of the flowpath), can measure the streamwise force according to the conservation of momentum $\mathrm{F}_{bx} = \Delta I$, where a negative gradient denotes drag, and a positive gradient denotes thrust. The impulse force can be generally divided into four stages: massive drag produced before the cowl notch at x=2.36 m and before the strut at x=3.4 m, mild drag produced before the nozzle at x=4.46 m, and thrust produced by the nozzle section. As illustrated in the H-K diagram (H for dimensionless static enthalpy and K for dimensionless kinetic energy), the deceleration and compression from the freestream condition to the burner entry condition by the combined means of isentropic compression and oblique shock waves would always increase the dimensionless stream thrust function. Pressure compression ratios ranging from 32 to 62 were produced by the current inlet as the freestream Mach number increases from 7 to 10. Note that frictionless, constant area heating implies a constant stream force function along the Rayleigh line. For the current nearly constant-area heating in the combustor section, the mild reduction in the stream force function is attributed to the friction drag. An excessive drag was produced when crossing the central strut, both by mechanical blocking and the Rayleigh heating effect. A small thrust indicted by the jump after the strut was due to the driving force of higher backpressure acted on the strut base. Thrust was mostly produced in the nozzle flowpath. An exception was the case of Mach 7 at 28 km, where the thrust was produced after the cowl notch as the flowpath is slightly expanded to connect the inlet and the combustor, and the combustion induced backpressure is large enough to push the isolator forward.

The dynamic pressure is found to correlate well with the mass capture rate, thrust, and drag, etc., as shown in Fig. 8 (a)-(c). It would be desirable to correlate the engine performance with a particular parameter(s). The mass capture rate is determined by resolving the coupling between the internal and external flows, while the global fuel equivalence ratio is automatically adjusted to maintain unity. The mass capture rate increases with dynamic pressure almost linearly below 30 kPa, and then takes a single sigmoid growth curve. The dependence can be well described by a gaussian function,

$$\dot{\mathrm{m}}_{air} = 1021.46\mathrm{e}^{-\left(\frac{q_0-111.9}{22.37}\right)^2} + 1.79365\mathrm{e}^{-\left(\frac{q_0-41.03}{23.17}\right)^2} \tag{20}$$

The aerodynamic force is obtained through integration over the engine surfaces for the pressure and viscous shear stress. In this study, the inviscid pressure force is always thrust, while the viscous friction force gives rise to drag. Net thrust is achieved only if the inviscid thrust exceeds the viscous drag. The inviscid thrust can be well fitted by a gaussian function,

$$F_{inv} = 3.286\times10^{17}e^{-\left(\frac{q_0-287}{40.14}\right)^2} + 1238e^{-\left(\frac{q_0-43.11}{23.94}\right)^2} \tag{21}$$

The curves of mass capture rate and the inviscid thrust are visually similar, and both follow the gaussian function. The plotting in Fig. 8 (d) suggests that the inviscid thrust is approximately scaled with the mass capture rate at a ratio of 658.2 m/s. The viscous friction drag increases roughly linearly with dynamic pressure as,

$$F_{vis} = 45.52q_0 - 522.7 \tag{22}$$

Due to the curved growth of inviscid thrust, net thrust is achieved for the low dynamic pressure range below 37 kPa and the high range above 55 kPa, while net drag is produced for the middle range. Similar to the mass capture rate, the peak pressure in the flow path can also be well correlated with dynamic pressure, as in Fig. 8 (c),

$$\dot{\mathrm{m}}_{air} = 6.474\times10^{16}\mathrm{e}^{-\left(\frac{q_0-214.7}{27.61}\right)^2} + 197.7\mathrm{e}^{-\left(\frac{q_0-43.85}{22.99}\right)^2} \tag{23}$$

Furthermore, the peak flowpath pressure is scaled with the mass capture rate at 101.5 s/m, as shown in Fig. 8 (d). As seen, the inviscid thrust performance is almost linearly determined by the mass capture rate, which is significantly influenced by the dynamic pressure. The mass capture rate is sensitive to the shock wave generated at the tip of the highly swept leading edges and the overboard flow spillage from the cowl closure. The hypersonic boundary layer along the compression ramp of the inlet grows more rapidly than at lower speeds (the thickness scales with the square of Mach number) and quickly becomes inordinately thick, as indicated by the high-temperature layer along the surfaces. Such a thick boundary layer exerts a nonnegligible displacement effect on the inviscid flow outside the boundary layer and causes more flow spillage from the cowl edge. The viscous skin friction and heat transfer are unwanted but must-be-considered effects for the inlet design, possibly by sophisticated CFD tests over a wide range of operating conditions.

4. Conclusions

The coupling between internal and external flows for a full-scale high-Mach scramjet was modeled by using high-fidelity Improved Delayed Detached Eddy Simulation (IDDES) together with a zone-based flamelet model (DZFM). The aim of this work is to provide some insights into the performance of high-Mach scramjets since the ground test facilities are generally unavailable. The utilized OpenFOAM-based numerical solver has been extensively validated for various scramjet cases previously, e.g., a similar high-Mach REST scramjet case, and the current modeling framework was further verified by using different mesh resolutions with 54.13 million, 71.76 million, 104.77 million, and 125.10 cells, respectively.

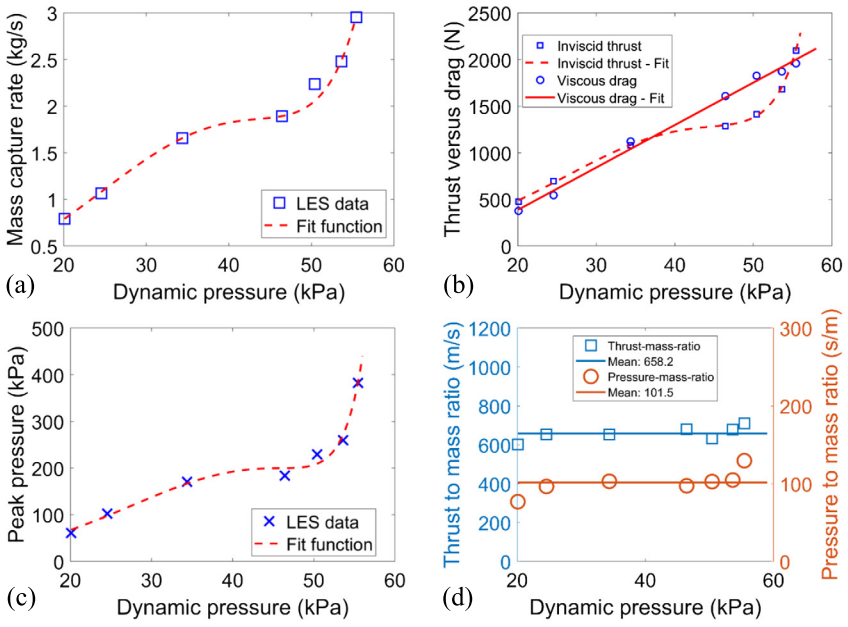

Fig. 8. Dependence of (a) mass capture, (b) inviscid thrust and viscous friction, (c) peak pressure, on dynamic pressure, (d) thrust-to-mass ration and pressure-to-mass ratio.

The numerical tests were conducted from the low hypersonic limit of 7 to 10. The engine performance can be well correlated with dynamic pressure. The mass capture rate, peak pressure, and inviscid thrust all increase with dynamic pressure nearly linearly below 30 kPa, and afterward take the single sigmoid pattern growth curve. In contrast, the viscous drag increases almost linearly with dynamic pressure. Due to the curved growth of inviscid thrust, net thrust is achieved when the inviscid thrust exceeds the viscous drag, i.e., for the low dynamic pressure range below 37 kPa and the high range above 55 kPa, while net drag is produced for the middle range. With the further increase of dynamic pressure, unstart occurs for the Mach 7 case operating at 28 km. Both the peak pressure and inviscid thrust scale with the mass capture rate at constant coefficients, suggesting that the uninstalled engine performance in a freestream condition is sensitive to the inlet, whose performance must be evaluated by including the viscous effect over a wide operating range.

Declaration of competing interest

The authors declare that they have no known competing financial interests or personal relationships that could have appeared to influence the work reported in this paper.

Acknowledgements

The research was supported by National Key Research and Development Program of China (2019YFB1704202), the Strategic Priority Research Program of Chinese Academy of Sciences (Grant No. XDA17030X00), and Training Program of the Major Research Plan of the National Natural Science Foundation of China (Grant No. 91641110). The authors are also grateful to the National Supercomputer Center in Tianjin for providing the computational resource.

References

[1] E.T. Curran, Scramjet engines: the first forty years, J. Propuls. Power 17 (6) (2001) 1138–1148, https://doi.org/10.2514/2.5875.
[2] G.Y. Anderson, An outlook on hypersonic flight, AIAA-87-2074, June 29-July 2, 1987.
[3] F. Falempin, M. Bouchez, M. Calabro, The microspace launcher: first step to the fully air-breathing space launcher, Prog. Propuls. Phys. (2011) 569–592, https://doi.org/10.1051/eucass/200901569.
[4] R. Rogers, A. Shih, C.Y. Tsai, R. Foelsche, Scramjet tests in a shock tunnel at flight Mach 7, 10, and 15 conditions, in: 37th Joint Propulsion Conference and Exhibit, 2001, https://doi.org/10.2514/6.2001-3241.
[5] L.A. Marshall, C. Bahm, G.P. Corpening, R. Sherrill, Overview with results and lessons learned of the X-43a Mach 10 flight, AIAA 2005-3336, 16-20 May 2005.
[6] M. Takahashi, K. Itoh, H. Tanno, T. Komuro, T. Sunami, K. Sato, S. Ueda, Study on the high speed scramjet characteristics at Ma 10 to 15 flight condition, 2005.
[7] J.M. Schramm, T. Sunami, K. Ito, K. Hannemann, Experimental investigation of supersonic combustion in the HIEST and HEG free piston driven shock tunnels, in: AIAA 2010-7122, Nashville, TN, 2010.
[8] Y. Wang, W. Shi, X. Wang, J. Zhang, J. Gao, J. Tang, J. Chang, W. Bao, Aerodynamic performance enhancement of a variable-geometry dual-mode combustor designed by the method of characteristics, Aerosp. Sci. Technol. 108 (2021), https://doi.org/10.1016/j.ast.2020.106353.
[9] V. Sharma, V. Eswaran, D. Chakraborty, Effect of location of a transverse sonic jet on shock augmented mixing in a scramjet engine, Aerosp. Sci. Technol. 96 (2020), https://doi.org/10.1016/j.ast.2019.105535.
[10] V. Sharma, V. Eswaran, D. Chakraborty, Determination of optimal spacing between transverse jets in a scramjet engine, Aerosp. Sci. Technol. 96 (2020), https://doi.org/10.1016/j.ast.2019.105520.
[11] S. Brahmachary, C. Fujio, H. Ogawa, Multi-point design optimization of a high-performance intake for scramjet-powered ascent flight, Aerosp. Sci. Technol. 107 (2020), https://doi.org/10.1016/j.ast.2020.106362.
[12] Z. Zhang, K. Ma, W. Zhang, X. Han, Y. Liu, Z. Jiang, Numerical investigation of a Mach 9 oblique detonation engine with fuel pre-injection, Aerosp. Sci. Technol. 105 (2020), https://doi.org/10.1016/j.ast.2020.106054.
[13] K. Kannaiyan, Numerical investigation of the local and global supersonic combustion characteristics of ethylene fuel, Aerosp. Sci. Technol. 106 (2020), https://doi.org/10.1016/j.ast.2020.106178.
[14] R.R. Shenoy, T.G. Drozda, A.T. Norris, R.A. Baurle, J.P. Drummond, Comparison of mixing characteristics for several fuel injectors at Mach 8, 12, and 15 hypervelocity flow conditions, July 9-11, 2018.
[15] R. Bakos, J. Tamagno, R. Trucco, O. Rizkalla, W. Chinitz, J.I. Erdos, Mixing and combustion studies using discrete orifice injection at hypervelocity flight conditions, J. Propuls. Power 8 (6) (1992) 1290–1296.
[16] M. Smart, E. Ruf, Free-jet testing of a rest scramjet at off-design conditions, in: 25th AIAA Aerodynamic Measurement Technology and Ground Testing Conference, San Francisco, California, 5-8 June 2006, https://doi.org/10.2514/6.2006-2955.
[17] W. Yao, Y. Yuan, X. Li, J. Wang, K. Wu, X. Fan, Comparative study of elliptic and round scramjet combustors fueled by Rp-3, J. Propuls. Power 34 (3) (2018) 772–786, https://doi.org/10.2514/1.B36721.
[18] M.K. Smart, Design of three-dimensional hypersonic inlets with rectangular-to-elliptical shape transition, J. Propuls. Power 15 (3) (1999) 408–416, https://doi.org/10.2514/2.5459.
[19] R. Gollan, P. Ferlemann, Investigation of rest-class hypersonic inlet designs, 11 - 14 April 2011, https://doi.org/10.2514/6.2011-2254.
[20] M.K. Smart, Experimental testing of a hypersonic inlet with rectangular-to-elliptical shape transition, J. Propuls. Power 17 (2) (2001) 276–283, https://doi.org/10.2514/2.5774.

[21] J.E. Barth, V. Wheatley, M.K. Smart, Effects of hydrogen fuel injection in a Mach 12 scramjet inlet, AIAA J. 53 (10) (2015) 2907–2919, https://doi.org/10.2514/1.J053819.
[22] A.D. Gardner, A. Paull, T.J. McIntyre, Upstream porthole injection in a 2-D scramjet model, Shock Waves 11 (2002) 369–375.
[23] W.Y.K. Chan, S.A. Razzaqi, J.C. Turner, M.V. Suraweera, M.K. Smart, Freejet testing of the HIFiRE 7 scramjet flowpath at Mach 7.5, J. Propuls. Power 34 (4) (2018) 844–853, https://doi.org/10.2514/1.B36652.
[24] D. Curran, V. Wheatley, M. Smart, Investigation of combustion mode control in a Mach 8 shape-transitioning scramjet, AIAA J. 57 (7) (2019) 2977–2988, https://doi.org/10.2514/1.J057999.
[25] M.V. Suraweera, M.K. Smart, Shock-tunnel experiments with a Mach 12 rectangular-to-elliptical shape-transition scramjet at offdesign conditions, J. Propuls. Power 25 (3) (2009) 555–564, https://doi.org/10.2514/1.37946.
[26] L.J. Doherty, M.K. Smart, D.J. Mee, Experimental testing of an airframe-integrated three-dimensional scramjet at Mach 10, AIAA J. 53 (11) (2015) 3196–3207, https://doi.org/10.2514/1.J053785.
[27] W.O. Landsberg, V. Wheatley, M.K. Smart, A. Veeraragavan, Enhanced supersonic combustion targeting combustor length reduction in a Mach 12 scramjet, AIAA J. (2019), https://doi.org/10.2514/1.J057417.
[28] J.E. Barth, Mixing and Combustion Enhancement in a Mach 12 Shape-Transitioning Scramjet Engine, PhD thesis, School of Mechanical and Mining Engineering, The University of Queensland, 2014.
[29] J.W. Dylan, K.S. Michael, Experimental investigation of a three-dimensional scramjet engine at Mach 12, in: 20th AIAA International Space Planes and Hypersonic Systems and Technologies Conference, Glasgow, Scotland, 6-9 July 2015, https://doi.org/10.2514/6.2015-3650.
[30] L.J. Doherty, M.K. Smart, D. Mee, Measurement of three-components of force on an airframe integrated scramjet at Mach 10, AIAA 2015-3523, 6-9 July 2015, https://doi.org/10.2514/6.2015-3523.
[31] T. Sunami, A. Murakami, K. Kudo, M. Kodera, M. Nishioka, Mixing and combustion control strategies for efficient scramjet operation in wide range of flight Mach number, AIAA 2002-5116, 29 September – 4 October 2002.
[32] H. Ogawa, M. Kodera, Physical insight into fuel/air mixing with hypermixer injectors for scramjet engines, J. Propuls. Power 31 (5) (2015) 1423–1435, https://doi.org/10.2514/1.B35638.
[33] A.S. Potturi, J.R. Edwards, LES/RANS simulation of a supersonic combustion experiment, in: 50th Aerospace Sciences Meeting Including the New Horizons Forum and Aerospace Exposition, Nashville, Tennessee, January 9-12, 2012.
[34] M. Saarlas, Reference temperature method for computing displacement thickness, AIAA J. 2 (11) (1964) 2056–2057, https://doi.org/10.2514/3.2741.
[35] U. Piomelli, Large-eddy and direct simulation of turbulent flows, in: Introduction to Turbulence Modelling, Von Karman Institute, Belgium, 2004.
[36] V. Sankaran, F. Genin, S. Menon, Subgrid mixing modeling for large eddy simulation of supersonic combustion, in: 42nd AIAA Aerospace Sciences Meeting and Exhibit, American Institute of Aeronautics and Astronautics, 2004.
[37] M. Dianat, Z. Yang, D. Jiang, J.J. McGuirk, Large eddy simulation of scalar mixing in a coaxial confined jet, Flow Turbul. Combust. 77 (1–4) (2006) 205–227, https://doi.org/10.1007/s10494-006-9044-4.
[38] W. Yao, On the application of dynamic zone flamelet model to large eddy simulation of supersonic hydrogen flame, Int. J. Hydrog. Energy 45 (41) (2020) 21940–21955, https://doi.org/10.1016/j.ijhydene.2020.05.189.
[39] A.Y. Klimenkoa, R.W. Bilger, Conditional moment closure for turbulent combustion, Prog. Energy Combust. Sci. 25 (1999) 595–687, https://doi.org/10.1016/S0360-1285(99)00006-4.
[40] E.E. O'Brien, T.-L. Jiang, The conditional dissipation rate of an initially binary scalar in homogeneous turbulence, Phys. Fluids 3 (12) (1991) 3121–3123.
[41] S.S. Girimaji, On the modeling of scalar diffusion in isotropic turbulence, Phys. Fluids 4 (11) (1992) 2529–2537.
[42] A. Kronenburg, R.W. Bilger, J.H. Kent, Computation of conditional average scalar dissipation in turbulent jet diffusion flames, Flow Turbul. Combust. 64 (2000) 145–159.
[43] S. Sreedhara, Y. Lee, K.Y. Huh, D.H. Ahn, Comparison of submodels for conditional velocity and scalar dissipation in CMC simulation of piloted jet and bluff-body flames, Combust. Flame 152 (1–2) (2008) 282–286, https://doi.org/10.1016/j.combustflame.2007.08.008.
[44] A. Cuoci, A. Frassoldati, T. Faravelli, E. Ranzi, Kinetic modeling of soot formation in turbulent nonpremixed flames, Environ. Eng. Sci. 25 (10) (2008) 1407–1422, https://doi.org/10.1089/ees.2007.0193.
[45] B. Thornber, R.W. Bilger, A.R. Masri, E.R. Hawkes, An algorithm for LES of premixed compressible flows using the conditional moment closure model, J. Comput. Phys. 230 (20) (2011) 7687–7705, https://doi.org/10.1016/j.jcp.2011.06.024.
[46] M. Cleary, J. Kent, Modelling of species in hood fires by conditional moment closure, Combust. Flame 143 (4) (2005) 357–368, https://doi.org/10.1016/j.combustflame.2005.08.013.
[47] K.J. Young, J.B. Moss, Modeling sooting turbulent jet flames using an extended flamelet technique, Combust. Sci. Technol. 105 (1995) 33–53.
[48] Y. Tominaga, T. Stathopoulos, Turbulent Schmidt numbers for CFD analysis with various types of flowfield, Atmos. Environ. 41 (37) (2007) 8091–8099, https://doi.org/10.1016/j.atmosenv.2007.06.054.
[49] J.D. Ott, C.K.K. Brinckman, S.M. Dash, Scramjet propulsive flowpath prediction improvements using recent modeling upgrades, in: 43rd Aerospace Sciences Meeting and Exhibition, Reno, Nevada, 2005.
[50] R.A. Baurle, D.R. Eklund, Analysis of dual-mode hydrocarbon scramjet operation at Mach 4–6.5, J. Propuls. Power 18 (5) (2002), https://doi.org/10.2514/2.6047.
[51] W. Yao, Y. Lu, K. Wu, J. Wang, X. Fan, Modeling analysis of an actively-cooled scramjet combustor under different kerosene/air ratios, J. Propuls. Power 34 (4) (2018) 975–991, https://doi.org/10.2514/1.B36866.
[52] M.L. Shur, P.R. Spalart, M.K. Strelets, A.K. Travin, A hybrid RANS-LES approach with delayed-DES and wall-modelled LES capabilities, Int. J. Heat Fluid Flow 29 (2008) 1638–1649, https://doi.org/10.1016/j.ijheatfluidflow.2008.07.0.
[53] P.R. Spalart, S.R. Allmaras, A one-equation turbulence model for aerodynamic flows, AIAA-92-0439, 6-9 January 1992, https://doi.org/10.2514/6.1992-439.
[54] O. Verhoeven, Trailing Edge Noise Simulations Using IDDES in Openfoam, Master thesis, Delft University of Technology, 2011.
[55] C.D. Pierce, P. Moin, A dynamic model for subgrid-scale variance and dissipation rate of a conserved scalar, Phys. Fluids 10 (12) (1998) 3041–3044.
[56] H. Zhang, A. Garmory, D.E. Cavaliere, E. Mastorakos, Large eddy simulation/conditional moment closure modeling of swirl-stabilized non-premixed flames with local extinction, Proc. Combust. Inst. 35 (2) (2015) 1167–1174, https://doi.org/10.1016/j.proci.2014.05.052.
[57] W. Yao, X. Fan, Development of zone flamelet model for scramjet combustor modeling, AIAA 2017-2277, 6-9 March 2017, https://doi.org/10.2514/6.2017-2277.
[58] W. Yao, B. Li, Application of dynamic zone flamelet model to a Gh2/Go2 rocket combustor, AIAA 2019-3868, 19-22 August 2019, https://doi.org/10.2514/6.2019-3868.
[59] A. Saghafian, V.E. Terrapon, H. Pitsch, An efficient flamelet-based combustion model for compressible flows, Combust. Flame 162 (3) (2015) 652–667, https://doi.org/10.1016/j.combustflame.2014.08.007.
[60] F. Ladeinde, Z. Lou, Improved flamelet modeling of supersonic combustion, J. Propuls. Power (2018), https://doi.org/10.2514/1.B36779.
[61] V.E. Terrapon, F. Ham, R. Pecnik, H. Pitsch, A flamelet-based model for supersonic combustion, in: 62th Annual Meeting of the APS Division of Fluid Dynamics, Minneapolis, 2009.
[62] Z. Gao, C. Jiang, C.-H. Lee, Representative interactive flamelet model and flamelet/progress variable model for supersonic combustion flows, Proc. Combust. Inst. 36 (2) (2017) 2937–2946, https://doi.org/10.1016/j.proci.2016.06.184.
[63] H.F. Mrema, G.V. Candler, Wall-modeled large eddy simulation of supersonic combustion using flamelet/progress-variable modeling, in: 2018 Joint Propulsion Conference, American Institute of Aeronautics and Astronautics, 2018.
[64] R. Vicquelin, B. Fiorina, S. Payet, N. Darabiha, O. Gicquel, Coupling tabulated chemistry with compressible CFD solvers, Proc. Combust. Inst. 33 (1) (2011) 1481–1488, https://doi.org/10.1016/j.proci.2010.05.036.
[65] Q. Jesse, G.D. Tomasz, C.M. James, L. Guilhem, C.O. Joseph, A priori analysis of a compressible flamelet model using RANS data for a dual-mode scramjet combustor, in: 22nd AIAA Computational Fluid Dynamics Conference, Dallas, TX, 22-26 June 2015, https://doi.org/10.2514/6.2015-3208.
[66] Y.P.d. Almeida, S. Navarro-Martinez, Large eddy simulation of a supersonic lifted flame using the Eulerian stochastic fields method, in: Proceedings of the Combustion Institute, 2018, https://doi.org/10.1016/j.proci.2018.08.040.
[67] Z. Huang, M.J. Cleary, H. Zhang, Application of the sparse-Lagrangian multiple mapping conditioning approach to a model supersonic combustor, Phys. Fluids 32 (9) (2020) 105120, https://doi.org/10.1063/5.0026654.
[68] C.J. Jachimowski, An Analysis of Combustion Studies in Shock Expansion Tunnels and Reflected Shock Tunnels, NASA Technical Paper 3224, Langley Research Center, Hampton, Virginia, 1992.
[69] E.B. James, J.W. Dylan, W. Vincent, K.S. Michael, Tailored fuel injection for performance enhancement in a Mach 12 scramjet engine, in: 20th AIAA International Space Planes and Hypersonic Systems and Technologies Conference, Glasgow, Scotland, 6-9 July 2015, https://doi.org/10.2514/6.2015-3614.
[70] R.J. Kee, F.M. Rupley, J.A. Miller, Chemkin-Ii: A Fortran Chemical Kinetics Package for the Analysis of Gas-Phase Chemical Kinetics, Sandia National Laboratories, 1989.
[71] M.W. Chase, NIST-JANAF thermochemical tables (4th ed.), J. Phys. Chem. Ref. Data 9 (1–2) (1998) 1–1952.
[72] R.B. Bird, W.E. Stewart, E.N. Lightfoot, Viscosity and the mechanisms of momentum transport, in: Transport Phenomena, 2nd edition, John Wiley & Sons, New York, 2002, p. 27.
[73] H.G. Weller, G. Tabor, H. Jasak, C. Fureby, A tensorial approach to CFD using object oriented techniques, Comput. Phys. 12 (6) (1997) 620–631, https://doi.org/10.1063/1.168744.
[74] Y. Lee, W. Yao, X. Fan, Low-dissipative hybrid compressible solver designed for large eddy simulation of supersonic turbulent flows, AIAA J. 56 (8) (2018) 3086–3096, https://doi.org/10.2514/1.J056404.
[75] A. Kurganov, S. Noelle, G. Petrova, Semidiscrete central-upwind schemes for hyperbolic conservation laws and Hamilton-Jacobi equations, SIAM J. Sci. Comput. 23 (3) (2001) 707–740, https://doi.org/10.1137/S1064827500373413.
[76] S. Pirozzoli, Generalized conservative approximations of split convective derivative operators, J. Comput. Phys. 229 (19) (2010) 7180–7190, https://doi.org/10.1016/j.jcp.2010.06.006.

[77] K. Wu, X. Li, W. Yao, X. Fan, Three-dimensional numerical study of the acoustic properties of a highly underexpanded jet, AIAA 2015-3572, 6-9 July 2015, https://doi.org/10.2514/6.2015-3572.
[78] X. Li, K. Wu, W. Yao, X. Fan, A comparative study of highly underexpanded nitrogen and hydrogen jets using large eddy simulation, AIAA 2015-3573, 6-9 July 2015, https://doi.org/10.2514/6.2015-3573.
[79] C.J. Greenshields, H.G. Weller, L. Gasparini, J.M. Reese, Implementation of semi-discrete, non-staggered central schemes in a colocated, polyhedral, finite volume framework, for high-speed viscous flows, Int. J. Numer. Methods Fluids 38 (2) (2009) 139–161, https://doi.org/10.1002/fld.2069.
[80] X. Li, W. Yao, X. Fan, Large-eddy simulation of time evolution and instability of highly underexpanded sonic jets, AIAA J. 54 (10) (2016) 3191–3211, https://doi.org/10.2514/1.J054689.
[81] X. Li, R. Zhou, W. Yao, X. Fan, Flow characteristic of highly underexpanded jets from various nozzle geometries, Appl. Therm. Eng. 125 (2017) 240–253, https://doi.org/10.1016/j.applthermaleng.2017.07.002.
[82] X. Li, E. Fan, W. Yao, X. Fan, Numerical investigation of characteristic frequency excited highly underexpanded jets, Aerosp. Sci. Technol. 63 (2017) 304–316, https://doi.org/10.1016/j.ast.2017.01.005.
[83] Y. Lee, W. Yao, X. Fan, A low-dissipation solver based on openfoam designed for large eddy simulation in compressible flows, AIAA 2017-2444, 6-9 March 2017, https://doi.org/10.2514/6.2017-2444.
[84] X. Li, K. Wu, W. Yao, X. Fan, A comparative study of highly underexpanded nitrogen and hydrogen jets using large eddy simulation, Int. J. Hydrog. Energy 41 (9) (2015) 5151–5161, https://doi.org/10.1016/j.ijhydene.2016.01.120.
[85] Y. Wang, K. Wu, W. Yao, X. Fan, Flow modulation and mixing enhancement of highly underexpanded jet by vortex excitation, AIAA J. 58 (6) (2020) 2462–2474, https://doi.org/10.2514/1.J058476.
[86] W. Yao, J. Wang, Y. Lu, X. Li, X. Fan, Full-scale detached eddy simulation of kerosene fueled scramjet combustor based on skeletal mechanism, AIAA 2015-3579, 6-9 July 2015, https://doi.org/10.2514/6.2015-3579.
[87] K. Wu, P. Zhang, W. Yao, X. Fan, Numerical investigation on flame stabilization in DLR hydrogen supersonic combustor with strut injection, Combust. Sci. Technol. 189 (12) (2017) 2154–2179, https://doi.org/10.1080/00102202.2017.1365847.
[88] W. Yao, Y. Lu, X. Li, J. Wang, X. Fan, Improved delayed detached eddy simulation of a high-ma active-cooled scramjet combustor based on skeletal kerosene mechanism, AIAA-2016-4761, 25-27 July 2016, https://doi.org/10.2514/6.2016-4761.
[89] K. Wu, W. Yao, X. Fan, Development and fidelity evaluation of a skeletal ethylene mechanism under scramjet-relevant conditions, Energy Fuels 31 (12) (2017) 14296–14305, https://doi.org/10.1021/acs.energyfuels.7b03033.
[90] W. Yao, K. Wu, X. Fan, Influences of domain symmetry on supersonic combustion modeling, J. Propuls. Power 35 (2) (2019) 451–465, https://doi.org/10.2514/1.B37227.
[91] Z. Huang, M. Zhao, Y. Xu, G. Li, H. Zhang, Eulerian-Lagrangian modelling of detonative combustion in two-phase gas-droplet mixtures with openfoam: validations and verifications, Fuel 286 (2021), https://doi.org/10.1016/j.fuel.2020.119402.
[92] H. Zhang, M. Zhao, Z. Huang, Large eddy simulation of turbulent supersonic hydrogen flames with openfoam, Fuel 282 (2020), https://doi.org/10.1016/j.fuel.2020.118812.
[93] C. Chelem, R. Groll, Magneto-plasmadynamic thruster modelling with coaxial induced magnetic field, Int. J. Comput. Methods Exp. Meas. 4 (4) (2016) 380–392, https://doi.org/10.2495/cmem-v4-n4-380-392.
[94] H. Stoldt, C.T. Johansen, A. Korobenko, P. Ziade, Verification and validation of a high-fidelity open-source simulation tool for supersonic aircraft aerodynamic analysis, in: AIAA Aviation 2020 Forum, Virtual Conference, June 15-19, 2020, https://doi.org/10.2514/6.2020-2758.
[95] W. Yao, L. Chen, Large eddy simulation of rest hypersonic combustor based on dynamic zone flamelet model, AIAA 2020-3722, August 24-28, 2020, https://doi.org/10.2514/6.2020-3722.
[96] R. Zhou, J.-P. Wang, Numerical investigation of flow particle paths and thermodynamic performance of continuously rotating detonation engines, Combust. Flame 159 (12) (2012) 3632–3645, https://doi.org/10.1016/j.combustflame.2012.07.007.
[97] H. Yamashita, M. Shimada, T. Takeno, A numerical study on flame stability at the transition point of jet diffusion flames, Proc. Combust. Inst. 26 (1) (1996) 27–34.
[98] T.F. Lu, C.S. Yoo, J.H. Chen, C.K. Law, Three-dimensional direct numerical simulation of a turbulent lifted hydrogen jet flame in heated coflow: a chemical explosive mode analysis, J. Fluid Mech. 652 (2010) 45–64, https://doi.org/10.1017/s002211201000039x.